bioRxiv preprint doi: https://doi.org/10.1101/199778; this version posted February 6, 2018. The copyright holder for this preprint (which was not certified by peer review) is the author/funder, who has granted bioRxiv a license to display the preprint in perpetuity. It is made available under aCC-BY-NC-ND 4.0 International license.

Visualizing acto-myosin dynamics and vortices at a membrane surface using interferometric scattering microscopy

Darius Köster[1,2,*], Nikolas Hundt[3], Gavin Young[3], Adam Fineberg[3], Philipp Kukura[3], Satyajit Mayor[1,4]

1 National Centre for Biological Sciences, Tata Institute for Fundamental Research, GKVK, Bellary Road, Bangalore 560065, India
2 Division of Biomedical Sciences, Warwick Medical School, University of Warwick, Coventry CV4 7AL, UK
3 Physical and Theoretical Chemistry Laboratory, Department of Chemistry, University of Oxford, South Parks Road, Oxford OX1 3QZ, UK
4 Institute for Stem Cell Biology and Regenerative Medicine, Bangalore 560065, India
* corresponding author: d.koester@warwick.ac.uk

Abstract

The plasma membrane and the underlying cytoskeletal cortex constitute active platforms for many cellular processes. Recent work has shown that acto-myosin dynamics modify the local membrane organization, but the molecular details are not well understood due to difficulties with experimentally accessing the relevant time and length scales. Here, we use interferometric scattering (iSCAT) microscopy to investigate a minimal acto-myosin network linked to a supported lipid bilayer membrane. Using the magnitude of the interferometric contrast, which is proportional to molecular mass, we detect, image and distinguish actin and myosin filaments. As a result, we can follow single, membrane attached actin filaments diffusing within the acto-myosin network, revealing differing types of motion depending on filament length. We go on to quantify myosin II filament dwell times and processivity as a function of ATP concentration, providing evidence for the predicted ensemble behavior of myosin head domains. Simultaneous observation of long-term network flow and organization enables us to link changes in myosin II filament dynamics with decreasing ATP concentrations to a switch in the acto-myosin network from a remodeling, fluid state to contractile behavior, and to observe the formation of vortices so far only predicted by theory.

Introduction

The acto-myosin cortex is critical for the mechanical stability of the cell and the organization of the adjacent plasma membrane. Several studies have shown that the cell cortex affects the dynamics and mobility of membrane components (1–3) and there is increasing evidence that the dynamic remodeling of the acto-myosin network drives the local concentration and clustering of membrane molecules (4–7). The complexity of the acto-myosin cortex and the plasma membrane in live cells, however, makes it difficult to study the molecular details of cortex-membrane interactions and to uncover dynamics of the underlying mechanisms. Reconstituted minimal systems provide a tractable way to studying the dynamics of a two-dimensional, membrane bound acto-myosin network, in which fluorescently labeled proteins are visualized using confocal or total internal reflection fluorescence (TIRF) microscopy (8–11).

These systems are of special interest, as they can adopt a range of active states depending on the ATP concentration, the actin to myosin ratio, the actin filament length and concentration (10, 11). Despite exhaustive experimental and theoretical analysis on the molecular and macroscopic level, the processes that lead from a remodeling, fluid-like acto-myosin network at high ATP concentrations to a contractile, solid-like network at low ATP concentrations remain poorly understood.

bioRxiv preprint doi: https://doi.org/10.1101/199778; this version posted February 6, 2018. The copyright holder for this preprint (which was not certified by peer review) is the author/funder, who has granted bioRxiv a license to display the preprint in perpetuity. It is made available under aCC-BY-NC-ND 4.0 International license.

Experimental approaches to studying myosin motor properties focuses largely on *in vitro* motility assays and optical tweezer studies, which have been used to probe the dynamics of single head domains. Recent advances in the theoretical understanding of myosin filament dynamics, which arise from multiple, interacting myosin head domains, indicate that small changes in the single head duty ratio in combination with the cooperative effects between the head domains can lead to a switch between non-processive and processive behavior of myosin II filaments (12–15). Corresponding experimental studies, however, are still missing. To address these outstanding issues, it is necessary to visualize the network components with a sub-second time-resolution over timescales of tens of minutes, which has been challenging to achieve with fluorescent probes due to photo-bleaching and photo-toxicity.

Here, we employed interferometric scattering (iSCAT) microscopy (16), a label-free imaging technique that relies on the interference between reflected and scattered light from nano-objects near an interface. The key advantages of light scattering over fluorescence detection in this context are the lack of an upper limit to fluorescence emission rate and the absence of photon absorption and thus photobleaching, enabling long observation times at high acquisition rates (> 1kHz). We measure microscopic quantities, such as actin filament diffusion rates, myosin filament dwell times and processivity, while simultaneously monitoring mesoscopic phenomena such as network flows and clustering. This allows us to link changes in the mechanochemical properties of myosin II filaments to transitions in the acto-myosin network, namely from the remodeling to the contractile state. Further, as predicted in theoretical studies of active polar matter (17, 18), we observe vortices during the transition into the contractile state, exhibiting persistent circular and spiral motion of myosin II filaments for minutes.

Results

Detection and characterization of actin and myosin filaments

The critical step to employ label-free imaging to study acto-myosin dynamics is establishing their detection, imaging and quantification. Due to the absence of any crowding factors or excess proteins, the actin and myosin II filaments were the principal sources of light scattering (Fig. 1A, B). First, we measured the signal of actin and myosin II filaments landing on bare glass slides, exhibiting contrasts of 0.058 ± 0.015 and 0.12 ± 0.013. The myosin II filaments exhibited an average length of 520 ± 130 nm (N=269) (Fig 1C; Sup Fig. 1A), in good agreement with earlier studies (10).

Given the much lower molecular mass of actin filaments (mass within a spot diameter of 313 nm: $m_{F\text{-}actin}$ / m_{myoII} = 4.8 MDa / 11.3 MDa = 0.42) (19), imaging of actin filaments requires subtraction of background signatures caused by cover glass roughness (see methods), after which we could visualize and track individual filaments (Fig. 1B; Sup Fig. 1B, C). Regions exhibiting consecutive deposition of actin filaments within a diffraction-limited spot, displayed a step-wise increase in the interferometric signal (Sup Fig. 1D, E; Video 1), in line with the scaling of the interferometric signal with molecular mass (20). These results suggest, that the iSCAT signal grows proportionally with the amount of protein in the region of interest even for large structures such as myosin filaments and can be translated into the number of actin filaments stacked on top of each other. Under the conditions used here ([G-actin] = 100-350 nM), we estimate that the actin layer is 1 to 6 filaments thick, with 2 filaments per diffraction-limited spot being most frequent (Sup Fig. 1F).

Mobility of actin filaments on supported lipid bilayers

bioRxiv preprint doi: https://doi.org/10.1101/199778; this version posted February 6, 2018. The copyright holder for this preprint (which was not certified by peer review) is the author/funder, who has granted bioRxiv a license to display the preprint in perpetuity. It is made available under aCC-BY-NC-ND 4.0 International license.

To check whether actin filaments linked to supported lipid bilayers (SLBs) are mobile and whether SLBs remain intact during the iSCAT measurements, we tracked the movement of individual actin filaments. Background subtraction to remove static actin network components revealed the mobile filament fraction and allowed us to identify and track single actin filaments using the characteristic contrast profile with constructive and destructive interference along the edge and center, respectively (Fig. 2A, B; Video 2). Our ability to follow the same filament at 10 Hz frame rate for several minutes, enabled us to determine the mean square displacement of the center of mass (MSD_{CM}) over three orders of magnitudes in the time domain. Short actin filaments (< 1.5 µm) exhibited free diffusion in the actin network, characterized by a linear increase of the MSD with time (logarithmic slope of 1) (Fig. 2C, D), whereas longer filaments (> 1.5µm) displayed a characteristic plateau. This suggests restricted mobility with a persistent orientation and a MSD trace indicative of confined diffusion with a logarithmic slope < 1; in line with the reptation of a flexible polymer within a meshwork (Fig 2D-F).

Binding dynamics of myosin II filaments to actin

We then characterized myosin II filament binding to membrane-bound actin at 100 µM ATP, which has been hypothesized to favor a remodeling network, and at 10 µM ATP, which leads to a contractile network, as described previously (11, 21). By creating kymographs along the tracks of myosin II filaments (Sup. Fig 3 A-C, Video 3), we find that the distribution of myosin II dwell times on F-actin can be described by a double-exponential decay function (Fig. 3A, E). At 100 µM ATP, the computed time constants were τ_{off1} = 1.23s (95% confidence interval 1.36 s -1.12 s) and τ_{off2} = 12.6 s (95% confidence interval 14 s - 11.3 s) with 69 % (95% confidence interval 66 %-71 %) of the events occurring with the short time, τ_{off1} (Fig. 3A). At 10 µM ATP, the myosin II filament dwell time constants were τ_{off1} = 3.7 s (95% confidence interval 3.1 s - 4.2 s) and τ_{off2} = 11.9 s (95% confidence interval 9.4 s - 15.5 s) with 77 % (95% confidence interval 63 % - 87 %) of the events displaying long dwell times characterized by τ_{off2} (Fig. 3E). We remark that these long dwell times are unlikely to be achieved by binding of single head domains, which have been reported to be on the ms timescale (22), but rather represent the concerted attachment of multiple head domains to actin filaments. The two phases of the double exponential distribution could, hence, be explained by the binding of either one or both sides of the bipolar myosin filament (Fig. 3I).

We went on to analyze the motion of myosin filaments bound to actin. At 100 µM ATP, the mobile myosin II filaments displayed a velocity distribution that can be described by a sum of two Gaussians with >60 % of myosin II filaments travelling at $v_{myoII,\,1}$ = 0.04 (±0.03) µm s^{-1} and the remaining at $v_{myoII,\,2}$ = 0.20 (±0.13) µm s^{-1} (Fig. 3B). The corresponding run length distribution decays exponentially with a characteristic run length of λ = 0.23 (±0.03) µm (Fig. 3C). Plotting run length versus attachment time shows a moderate positive correlation (Pearson coefficient 0.38) for dwell times < 3 s and a weak negative correlation (Pearson coefficient -0.17) for longer binding times. This implies that the population corresponding to short dwell times is mobile while the population with long dwell times exhibits slow, reduced motion and eventually becomes immobilized (Fig. 3D, Sup Fig. 3D).

At 10 µM ATP, when the network becomes contractile and myosin II filament dwell times are longer, the mobile myosin II filaments travel with an average velocity of v_{myoII} = 0.46 (±0.20) µm s^{-1} (Fig. 3F, single Gaussian distribution) and the characteristic run length is λ = 1.03 (±0.05) µm (Fig. 3G). The correlation between run length and dwell time is stronger than at 100 µM ATP with most myosin II filaments exhibiting persistent motion for up to 6 s (Pearson coefficient 0.57) and a loss of this correlation at longer dwell times (Pearson coefficient -0.18) (Fig 3H). We emphasize that the myosin II filament motion

bioRxiv preprint doi: https://doi.org/10.1101/199778; this version posted February 6, 2018. The copyright holder for this preprint (which was not certified by peer review) is the author/funder, who has granted bioRxiv a license to display the preprint in perpetuity. It is made available under aCC-BY-NC-ND 4.0 International license.

is more persistent and faster at 10 µM ATP as compared to 100 µM ATP in agreement with recent theoretical studies (15, 23). These results suggest that increased processivity and dwell time with decreasing ATP concentrations provides a molecular mechanism underlying the transition from a remodeling to a contractile acto-myosin network.

Characterization of acto-myosin network dynamics

Having established that we can characterize myosin and actin filament dynamics, as well as distinguishing between the two based on iSCAT contrast, we chose to study the full network dynamics, in the remodeling state at 100 µM ATP and the contractile state at 10 µM ATP (11). Since long-term imaging neither affected the activity of myosin filaments nor the integrity of actin filaments, we were able to observe the transition from a homogeneous network (t = [1-4min]) via the formation of small clusters (t = [7-10 min]) to large cluster formation (t = [13-16 min]) as ATP becomes depleted with time (Fig. 4A, Video 4). To visualize myosin II filament action on the actin network with decreasing ATP concentrations, we computed the standard deviation of the interferometric signal over the time sequences depicted in Fig. 4A. The remodeling acto-myosin network (100 µM ATP) is characterized by small values of the standard deviation that is spatially homogeneous, whereas small regions (2 µm diameter) with high signal variation begin to appear at t = [7-10min]. These grow and fuse to form larger regions of 5-10 µm diameter when the system runs out of ATP at t = [13-16 min] (Fig. 4B).

To analyze the myosin II generated flows of the acto-myosin network in the remodeling and contractile states, and to identify regions of clustering, we performed particle image velocimetry (PIV) resulting in vector fields corresponding to the overall flow velocities of the acto-myosin network. The contractile regions observed in the contractile state of the network display increased material inflow, which translated into a local negative divergence of the velocity field as seen in the contractile state at low ATP (Fig. 4C, D). In contrast, the network in the remodeling state does not exhibit large-scale flows and does not generate contractile regions (Fig. 4E, F). The average network velocities are higher in the contractile state, $v_{network}$ = 74 (±64) nm s^{-1} compared to $v_{network}$ = 14 (±14) nm s^{-1} in the remodeling state (Fig. 4G). This result correlates with our observations on myosin II dynamics in that short interactions of myosin II filaments with actin at 100 µM ATP (Fig. 3C-F) lead to minor changes of the network in the remodeling state, whereas longer interaction times and more persistently moving myosin II filaments at 10 µM ATP (Fig. 3G-J) result in faster network velocities, potentially resulting in the contractile state.

Sustained vortex formation by the acto-myosin network

Remarkably, in experiments with long actin filaments (300 nM actin, 80 nM myosin II) we observed the formation of spirals and vortices of the acto-myosin network after transitioning from the remodeling state into the contractile state (Fig. 5A, Video 5). Vortex formation is expected for active gels of polar filaments (17, 18, 24), and our observations support the notion that the intrinsic properties of actin filaments and myosin motors lead to the formation of stable vortices. These vortices typically comprised multiple myosin II filaments moving circularly around a common point with radii of 1-5 µm and remained stable for several minutes. PIV on single vortices showed a circular flow, mainly of myosin II filaments, around the center with a velocity profile that peaks at about half of the vortex radius (Fig. 5B, C), in good agreement with theoretical work (17, 18). We observed vortices with a static center position that were stable for minutes (Video 5 and 6) as well as transient vortices that merged into larger, contractile structures (Video 7).

bioRxiv preprint doi: https://doi.org/10.1101/199778; this version posted February 6, 2018. The copyright holder for this preprint (which was not certified by peer review) is the author/funder, who has granted bioRxiv a license to display the preprint in perpetuity. It is made available under aCC-BY-NC-ND 4.0 International license.

Discussion

The study of myosin II filament dynamics on actin filaments inside the membrane-bound, remodeling acto-myosin network provides new insights of how network dynamics on the mesoscale are related to minute changes of the physico-chemical properties of myosin II motors on the single-filament scale. Our approach allowed us to determine that a change in myosin II filament dwell times from $\tau_{1,100\mu M\ ATP}$ = 1.23 s to $\tau_{1,10\mu M\ ATP}$ = 3.7 s switches the acto-myosin network from a remodeling to a contractile state, and that myosin II filaments move faster and more processively at 10 µM ATP. This effect of ATP concentration on myosin II filaments under load provides evidence for predictions made by theoretical studies (15, 23). Our observations indicate that the control of myosin dwell times could provide an ideal way for a biological system to switch between a remodeling or fluid-like network state to a contractile or solid-like state. Short dwell times of myosin filaments limit the persistence of myosin motion, as well as the number of actin filaments that are crosslinked by myosin filaments. In this regime, the action of a single myosin filament is spatially confined, and the acto-myosin network is in a locally remodeling, fluctuating state without large-scale contraction. In contrast, long dwell times and persistent motion of myosin filaments increase the connectivity of the acto-myosin network and promote the transmission of stress over longer distances, leading to a globally contractile state (25). Control of network crosslinking timescales as a way to change network rheology and its relevance for the understanding of human diseases was also shown for the actin cross linker alpha-actinin (26). Our study demonstrates how iSCAT microscopy will be useful in the future to capture the dynamics of entire networks made from more components than just acto-myosin.

In addition, our results reveal two populations of interactions between actin and myosin II filaments, i.e. short interactions on the order of τ_{off1} (1.23 s at 100 µM ATP and 3.7 s at 10 µM ATP) and the other with long interactions on the order of τ_{off2} (12.6 s at 100 µM ATP and 11.9 s at 10 µM ATP). Compared to the dwell time of a single myosin head domain of 25-40 ms, the observed dwell times are much longer and probably represent the concerted binding of multiple myosin head domains of the same filament (15, 27). It remains to be elucidated what the nature of the two dwell time populations is. The head domains in a myosin II filament are arranged in a bipolar structure, i.e. both ends are enriched with myosin heads and a thin, bare stalk made from the tail domains connects the two ends. One possibility is that short dwell times represent attachments of multiple heads of one filament end to an actin filament and longer dwell times represent binding of both myosin filament ends to actin. The observation that many of the myosin II filaments with long dwell times show only little motion supports the notion that the myosin filament binds and connects two, anti-parallel actin filaments resulting in the stalling of the myosin motion (Fig. 3 K). In the future, more detailed studies using non-muscle myosin II isoforms which allow tight control of the number of functional head domains (28) will be ideal to test the nature of the longer binding times as well as the theoretically predicted differences at low ATP concentrations between muscle and non-muscle myosin II filaments (15).

Beyond the dynamics of individual actin and myosin filaments, we used PIV to detect acto-myosin network flows and relate regions of high activity to individual myosin II filament dynamics. We find that contractile regions display an acto-myosin flow field with negative divergence, i.e. the center of the contractile regions act as sinks for material flow (17, 29). Interestingly, these contractile regions are stable on a time scales of hundreds of seconds and seem to constitute a steady state where myosin II filaments continue to travel towards existing myosin clusters and detach before getting jammed in the cluster. This observation of sustained flows of myosin motors along a preformed, myosin stabilized actin structure could be an *in vitro* reconstruction of regions showing sustained membrane protein clustering for tens of seconds on the

bioRxiv preprint doi: https://doi.org/10.1101/199778; this version posted February 6, 2018. The copyright holder for this preprint (which was not certified by peer review) is the author/funder, who has granted bioRxiv a license to display the preprint in perpetuity. It is made available under aCC-BY-NC-ND 4.0 International license.

plasma membrane of living cells which are thought to be driven by the formation of contractile acto-myosin platforms (30, 31).

The observation of vortices represents another active steady state that was predicted in theoretical work on active gels (17, 18). It is interesting to note that such structures were not observed by earlier studies using TIRF microscopy and similar reconstituted systems (11, 32, 33). Recently, vortices were observed in freshly adhering cells by the use of enhanced TIRF structural illumination microscopy, but the mechanism of vortex formation remained unclear (34). The present work indicates that vortices can indeed occur solely based on the action of myosin II filaments on actin filaments and further studies are necessary to clarify this topic.

Materials and Methods

Purified Proteins

Actin was purified from chicken breast following the protocol from Spudich and Watt (35) and kept on ice in monomeric form in G-buffer (2 mM Tris Base, 0.2 mM ATP, 0.5 mM TCEP-HCl, 0.04% NaN_3, 0.1 mM CaCl2, pH 7.0); Myosin II was obtained from chicken breast following a modified protocol from Pollard (36) and kept in monomeric form in myo-buffer (500 mM KCl, 1 mM EDTA, 1 mM DTT, 10 mM HEPES, pH 7.0). The day prior to experiments, functional myosin II proteins are separated from proteins containing dead head domains by a round of binding and unbinding to F-actin at a 5:1 actin to myosin ratio (switch from no ATP to 3 mM ATP) followed by a spin at 60,000 rpm for 10 min at 4 ^{o}C in a TLA100.3 rotor. The supernatant containing functional myosin II is dialyzed against myo-buffer over-night and used for experiments for up to three days.

To link actin to the SLB, we used a construct containing 10x His domains followed by a linker (KCK) and the actin binding domain of Ezrin (HKE) as described earlier (11).

Supported Lipid Bilayer and Experimental Chamber Preparation

Glass coverslips (#1.5 borosilicate, Menzel, Germany) for SLB formation were cleaned with Hellmanex III (Hellma Analytics, Mühlheim, Germany) following the manufacturer's instructions followed by thorough rinses with EtOH and MilliQ water, blow dried with N_2 and finally passed briefly over a Bunsen burner flame. For the experimental chamber, 0.2 ml PCR tubes (Tarsons Products, Kolkata, India) were cut to remove the lid and the conical bottom part and stuck to the cleaned glass using UV glue (NOA88, Norland Products, Cranbury, NJ) and three minutes curing by intense UV light at 365 nm (PSD-UV8T, Novascan, Ames, IA). Freshly cleaned and assembled chambers were directly used for experiments.

Supported lipid bilayers (SLB) were formed by fusion of small uni-lamellar vesicles (SUV). Lipid mixtures containing 98% DOPC and 2% DGS-NTA(Ni^{2+}) were mixed together with 1 ml chloroform (Electron Microscopy Sciences, Hatfield, PA) in a cleaned amber glass vial (B7990-2A, Thermo Fisher Scientific, Rockwood, TN), dried under a N_2 stream, placed in a vacuum desiccator overnight and resuspended in SUV storage buffer (150 mM NaCl, 20 mM HEPES, 5% sucrose, pH 7.2) to a final lipid concentration of 4 mM. SUVs of ~80 nm diameter were formed by the extrusion method using a lipid extruder (Avanti Polar Lipids Inc.) with an 80 nm pore size polycarbonate filter membrane (GE Whatman, Piscataway, NJ).

For SLB formation, 10-20 µl of SUV mix were added to 100 µl of SLB formation buffer (150 mM NaCl, 2 mM $CaCl_2$, 20 mM HEPES, pH 5.5), incubated for 20 min at RT and washed ten times with SLB working

bioRxiv preprint doi: https://doi.org/10.1101/199778; this version posted February 6, 2018. The copyright holder for this preprint (which was not certified by peer review) is the author/funder, who has granted bioRxiv a license to display the preprint in perpetuity. It is made available under aCC-BY-NC-ND 4.0 International license.

buffer (150 mM NaCl, 20 mM HEPES, 0.1 mg/ml κ-casein, pH 7.2). For experiments with F-actin, SLB working buffer was replaced by 100 µl KMEH (50 mM KCl, 2 mM $MgCl_2$, 1 mM EGTA, 20 mM HEPES, pH 7.2).

Formation of Acto-Myosin Network

In a typical experiment, SLBs were incubated with 10 nM HKE for 40 min and washed thrice with KMEH. During this incubation time, F-actin was polymerized. First10%$_{vol}$ of 10x ME buffer (100 mM MgCl2, 20 mM EGTA, pH 7.2) were mixed with the G-actin stock and incubated for 2 min to replace G-actin bound Ca^{2+} ions with Mg^{2+}. Addition of 2x KMEH buffer supplemented with 2 mM Mg-ATP induced F-actin polymerization at a final G-actin concentration of 5 µM. After 20-30 min incubation, the desired amount of F-actin was added to the SLBs using blunt cut 200 µl pipette tips. An incubation of 30 min allowed the F-actin layer to bind to the SLB at steady-state, myosin II filaments were added afterwards and the evolution of the acto-myosin system was observed for up to 90 min. To induce remodeling of the acto-myosin system, Mg-ATP (100 mM) was added to a final concentration of 1 mM. Each step of this procedure was performed on the microscope stage, which allowed us to check its state continuously. The open chamber design allowed the addition of each component from top without induction of flows that would perturb the actin network.

iSCAT microscopes

Interferometric scattering microscopy was performed on two different home-built setups similar to those detailed in (37, 38). Briefly, a weakly focused laser beam was scanned across the sample over an area of 24 x 24 µm^2 (445 nm laser) or 32.6 x 32.6 µm^2 (635 nm laser). The light reflected from the glass-water interface together with the scattered light from the sample was imaged onto a CMOS camera (445 nm laser: Point Grey GS3-U3-23S6M-C, Flir, Canada; 635 nm laser: MV-D1024-160-CL-8, Photonfocus, Switzerland). The cameras were controlled using home-written LabVIEW software. The setup with the 445 nm laser had a 3.5 mm partially reflective mirror placed in the re-imaged back focal plane of the objective for enhanced scattering contrast as described in (38). The videos were recorded at 10 fps (445 nm laser) and 5 fps (635 nm laser) with the illumination intensity on the sample (445 nm laser: 250 W/cm2; 635 nm laser: 1.9 kW/cm2) set to nearly saturate the camera with the returning light. The pixel sizes were 23.4 nm/pixel (445 nm laser) and 31.8 nm/pixel (635 nm laser).

Image processing

Non-sample specific illumination inhomogeneities, fixed-pattern noise and constant background were removed from the raw images by dividing each of them with a flat field image that contained only these features. The flat field image was computed by recording 2000 frames of the sample while moving the stage. For each pixel, a temporal median was calculated resulting in a flat field image that only contained static features.

Median filtering

bioRxiv preprint doi: https://doi.org/10.1101/199778; this version posted February 6, 2018. The copyright holder for this preprint (which was not certified by peer review) is the author/funder, who has granted bioRxiv a license to display the preprint in perpetuity. It is made available under aCC-BY-NC-ND 4.0 International license.

Movies were median filtered using MATLAB (MathWorks, Natick, MA, USA). For each image sequence, the median is computed for each pixel, deleted from the original image sequence and the median filtered image sequence as well as the computed median filter are saved.

Actin filament tracking

Actin filaments that became visible after median filtering and that did not cross other actin filaments for at least 1000 frames were tracked using image J (http://imagej.nih.gov) and the plugin JFilament (http://athena.physics.lehigh.edu/jfilament). The obtained tracking traces were analyzed using MATLAB to compute the position of the center of mass (CM) for each time point and to generate plots of the CMs mean square displacement.

Myosin length measurements

Intensity line-scans along the long axis of single myosin filaments were taken and the distance between the half maximum points at both ends were taken as the length of the myosin II filament.

Myosin binding dynamics

Imaging with 5-10 Hz for several minutes was sufficient to capture a broad range of myosin filament dynamics with high accuracy. To remove any signal originating from static structures such as immobile actin filaments or small impurities in the SLB, the image sequences were median filtered (16). In a second step, a maximum projection of the time series was used to visualize the tracks occupied by myosin II filaments during the experiment. Lines following these tracks were then used to compute kymographs depicting the myosin II filament binding times and their motion along actin filaments (kymograph tool in Image J, line width 3). The measured dwell time, run length and velocity distributions were plotted and further analyzed using OriginPro 2016 (OriginLab Corporation, Northampton, MA, USA) and MATLAB. Best fitting functions for the myosin II filament dwell times were selected using MEMLET, that estimates the maximum likelihood of a fitting function to describe a data point distribution (39).

Particle Image Velocimetry

Particle Image Velocimetry (PIV) was performed using PIVlab (40, 41) (Garcia, D. (2011): A fast all-in-one method for automated post-processing of PIV data. Experiments in Fluids, Springer-Verlag, 2011, 50, 1247-1259). Median filtered image sequences were inverted and transformed into 8-bit format using Image J. The PIV vector maps were computed with the FFT window deformation algorithm and the window sizes of 64, 32 and 16 pixels and step sizes of 32, 16 and 8 pixels, respectively. The accepted range of velocity vectors was limited to ± 2 µm s^{-1}. *Intensity autocorrelation*

Image sequences were inverted before the intensity autocorrelation, $\chi(\vec{x}) = < \delta_l(\vec{y})\delta_l(\vec{y}+\vec{x}) >$, was computed in MATLAB with a fast Fourier transform and summed over the angular coordinate to obtain χ(r).

bioRxiv preprint doi: https://doi.org/10.1101/199778; this version posted February 6, 2018. The copyright holder for this preprint (which was not certified by peer review) is the author/funder, who has granted bioRxiv a license to display the preprint in perpetuity. It is made available under aCC-BY-NC-ND 4.0 International license.

Contributions:

DK conceived, designed and performed experiments, analyzed data, wrote manuscript; NH helped in the experiments, analyzed data, wrote manuscript; GY and AF built the iSCAT microscopes; PK conceived experiments, wrote manuscript; SM conceived experiments, wrote manuscript.

Acknowledgements

DK thanks Madan Rao and Kabir Husain (NCBS) for instructive discussions and comments on the manuscript and the Company of Biologists for supporting this work with a Travelling fellowship. NH thanks James Sellers and Yasuharu Takagi from the NIH for providing the actin. DK was a Campus Fellow at NCBS; NH was supported by DFG research fellowship, grant HU 2462/1-1. GY was supported by a Zvi and Ofra Meitar Magdalen Graduate Scholarship; PK was supported by an ERC Starting Investigator Grant (Nanoscope, 337577); This work was supported by a JC Bose Fellowship from the Department of Science and Technology, a Margadarshi Fellowship IA/M/15/1/502018 (Wellcome Trust–Department of Biotechnology, India Alliance), from the Government of India (SM).

References:

1. Kusumi, A., C. Nakada, K. Ritchie, K. Murase, K. Suzuki, H. Murakoshi, R.S. Kasai, J. Kondo, T. Fujiwara, and HidejiMurakoshi. 2005. Paradigm shift of the plasma membrane concept from the two-dimensional continuum fluid to the partitioned fluid: high-speed single-molecule tracking of membrane molecules. Annu. Rev. Biophys. Biomol. Struct. 34: 351–78.

2. Arumugam, S., and P. Bassereau. 2015. Membrane nanodomains: contribution of curvature and interaction with proteins and cytoskeleton. Essays Biochem. 57: 109–19.

3. Saka, S.K., A. Honigmann, C. Eggeling, S.W. Hell, T. Lang, and S.O. Rizzoli. 2014. Multi-protein assemblies underlie the mesoscale organization of the plasma membrane. Nat. Commun. 5: 1–14.

4. Rao, M., and S. Mayor. 2014. Active organization of membrane constituents in living cells. Curr. Opin. Cell Biol. 29C: 126–132.

5. van Zanten, T.S., A. Cambi, M. Koopman, B. Joosten, C.G. Figdor, M.F. Garcia-Parajo, and T.S. Van Zanten. 2009. Hotspots of GPI-anchored proteins and integrin nanoclusters function as nucleation sites for cell adhesion. Proc. Natl. Acad. Sci. U. S. A. 106: 18557–62.

6. Plowman, S.J., C. Muncke, R.G. Parton, and J.F. Hancock. 2005. H-ras, K-ras, and inner plasma membrane raft proteins operate in nanoclusters with differential dependence on the actin cytoskeleton. Proc. Natl. Acad. Sci. U. S. A. 102: 15500–5.

7. Köster, D. V, and S. Mayor. 2016. Cortical actin and the plasma membrane: inextricably intertwined. Curr. Opin. Cell Biol. 38: 81–89.

8. Murrell, M.P., and M.L. Gardel. 2012. F-actin buckling coordinates contractility and severing in a biomimetic actomyosin cortex. Proc. Natl. Acad. Sci. U. S. A. .

9. Vogel, S.K., F. Heinemann, G. Chwastek, and P. Schwille. 2013. The design of MACs (minimal actin cortices). Cytoskeleton. 70: 706–717.

bioRxiv preprint doi: https://doi.org/10.1101/199778; this version posted February 6, 2018. The copyright holder for this preprint (which was not certified by peer review) is the author/funder, who has granted bioRxiv a license to display the preprint in perpetuity. It is made available under aCC-BY-NC-ND 4.0 International license.

10. Ideses, Y., A. Sonn-Segev, Y. Roichman, and A. Bernheim-Groswasser. 2013. Myosin II does it all: assembly, remodeling, and disassembly of actin networks are governed by myosin II activity. Soft Matter. 9: 7127.

11. Köster, D.V., K. Husain, E. Iljazi, A. Bhat, P. Bieling, R.D. Mullins, M. Rao, and S. Mayor. 2016. Actomyosin dynamics drive local membrane component organization in an in vitro active composite layer. Proc. Natl. Acad. Sci. 113: E1645–E1654.

12. Bidone, T.C., W. Jung, D. Maruri, C. Borau, R.D. Kamm, and T. Kim. 2017. Morphological Transformation and Force Generation of Active Cytoskeletal Networks. PLoS Comput. Biol. 13: e1005277.

13. Albert, P.J., T. Erdmann, and U.S. Schwarz. 2014. Stochastic dynamics and mechanosensitivity of myosin II minifilaments. New J. Phys. 16.

14. Rastogi, K., M.S. Puliyakodan, V. Pandey, S. Nath, and R. Elangovan. 2016. Maximum limit to the number of myosin II motors participating in processive sliding of actin. Sci. Rep. 6: 32043.

15. Erdmann, T., K. Bartelheimer, and U.S. Schwarz. 2016. Sensitivity of small myosin II ensembles from different isoforms to mechanical load and ATP concentration. Phys. Rev. E. 94: 1–9.

16. Ortega Arroyo, J., D. Cole, and P. Kukura. 2016. Interferometric scattering microscopy and its combination with single-molecule fluorescence imaging. Nat. Protoc. 11: 617–633.

17. Kruse, K., J.F. Joanny, F. Julicher, J. Prost, and K. Sekimoto. 2004. Asters , Vortices , and Rotating Spirals in Active Gels of Polar Filaments. Phys. Rev. Lett. 92: 1–4.

18. Husain, K., and M. Rao. 2017. Emergent Structures in an Active Polar Fluid: Dynamics of Shape, Scattering, and Merger. Phys. Rev. Lett. 118: 1–5.

19. AL-Khayat, H.A. 2013. Three-dimensional structure of the human myosin thick filament: Clinical implications. Glob. Cardiol. Sci. Pract. 2013: 36.

20. Young, G., N. Hundt, D. Cole, A. Fineberg, J. Andrecka, A. Tyler, A. Olerinyova, A. Ansari, E.G. Marklund, M.P. Collier, S.A. Chandler, O. Tkachenko, J. Allen, M. Crispin, N. Billington, Y. Takagi, J.R. Sellers, C. Eichmann, P. Selenko, L. Frey, R. Riek, M.R. Galpin, W.B. Struwe, J.L.P. Benesch, and P. Kukura. 2017. Quantitative mass imaging of single molecules in solution. bioRxiv. : 229740.

21. Smith, D., F. Ziebert, D. Humphrey, C. Duggan, M. Steinbeck, W. Zimmermann, and J. Käs. 2007. Molecular motor-induced instabilities and cross linkers determine biopolymer organization. Biophys. J. 93: 4445–52.

22. Baker, J.E., C. Brosseau, P.B. Joel, and D.M. Warshaw. 2002. The biochemical kinetics underlying actin movement generated by one and many skeletal muscle myosin molecules. Biophys. J. 82: 2134–2147.

23. Stam, S., J. Alberts, M.L. Gardel, and E. Munro. 2015. Isoforms confer characteristic force generation and mechanosensation by myosin II filaments. Biophys. J. 108: 1997–2006.

24. Nédélec, F.J., T. Surrey, A.C. Maggs, and S. Leibler. 1997. Self-organization of microtubules and motors. Nature. 389: 305–8.

25. Alvarado, J., M. Sheinman, A. Sharma, F.C. MacKintosh, and G.H. Koenderink. 2013. Molecular motors robustly drive active gels to a critically connected state. Nat. Phys. 9: 1–7.

bioRxiv preprint doi: https://doi.org/10.1101/199778; this version posted February 6, 2018. The copyright holder for this preprint (which was not certified by peer review) is the author/funder, who has granted bioRxiv a license to display the preprint in perpetuity. It is made available under aCC-BY-NC-ND 4.0 International license.

26. Ehrlicher, A.J., R. Krishnan, M. Guo, C.M. Bidan, D.A. Weitz, and M.R. Pollak. 2015. Alpha-actinin binding kinetics modulate cellular dynamics and force generation. Proc. Natl. Acad. Sci. 112: 6619–6624.

27. Kovács, M., J. Tóth, C. Hetényi, A. Málnási-Csizmadia, and J.R. Seller. 2004. Mechanism of blebbistatin inhibition of myosin II. J. Biol. Chem. 279: 35557–35563.

28. Billington, N., A. Wang, J. Mao, R.S. Adelstein, and J.R. Sellers. 2013. Characterization of three full-length human nonmuscle myosin II paralogs. J. Biol. Chem. 288: 33398–33410.

29. Gowrishankar, K., and M. Rao. 2015. Nonequilibrium phase transitions, fluctuations and correlations in an active contractile polar fluid. Soft Matter. 1201.3938.

30. Gowrishankar, K., S. Ghosh, S. Saha, R. C, S. Mayor, and M. Rao. 2012. Active remodeling of cortical actin regulates spatiotemporal organization of cell surface molecules. Cell. 149: 1353–67.

31. Goswami, D., K. Gowrishankar, S. Bilgrami, S. Ghosh, R. Raghupathy, R. Chadda, R. Vishwakarma, M. Rao, and S. Mayor. 2008. Nanoclusters of GPI-anchored proteins are formed by cortical actin-driven activity. Cell. 135: 1085–97.

32. Murrell, M., and M.L. Gardel. 2014. Actomyosin sliding is attenuated in contractile biomimetic cortices. Mol. Biol. Cell. 25: 1845–53.

33. Vogel, S.K., Z. Petrasek, F. Heinemann, and P. Schwille. 2013. Myosin motors fragment and compact membrane-bound actin filaments. Elife. 2: 1–18.

34. Fritzsche, M., D. Li, H. Colin-York, V.T. Chang, E. Moeendarbary, J.H. Felce, E. Sezgin, G. Charras, E. Betzig, and C. Eggeling. 2017. Self-organizing actin patterns shape membrane architecture but not cell mechanics. Nat. Commun. 8: 14347.

35. Spudich, J.A., and S. Watt. 1971. The regulation of rabbit skeletal muscle contraction. I. Biochemical studies of the interaction of the tropomyosin-troponin complex with actin and the proteolytic fragments of myosin. J. Biol. Chem. 246: 4866–71.

36. Pollard, T.D. 1982. Myosin purification and characterization. Methods Cell Biol. 24: 333–71.

37. Ortega-Arroyo, J., and P. Kukura. 2012. Interferometric scattering microscopy (iSCAT): new frontiers in ultrafast and ultrasensitive optical microscopy. Phys. Chem. Chem. Phys. 14: 15625.

38. Cole, D., G. Young, A. Weigel, A. Sebesta, and P. Kukura. 2017. Label-Free Single-Molecule Imaging with Numerical-Aperture-Shaped Interferometric Scattering Microscopy. ACS Photonics. 4: 211–216.

39. Woody, M.S., J.H. Lewis, M.J. Greenberg, Y.E. Goldman, and E.M. Ostap. 2016. MEMLET: An Easy-to-Use Tool for Data Fitting and Model Comparison Using Maximum-Likelihood Estimation. Biophys. J. 111: 273–282.

40. Thielicke, W., and E.J. Stamhuis. 2014. PIVlab – Towards User-friendly, Affordable and Accurate Digital Particle Image Velocimetry in MATLAB. J. Open Res. Softw. 2.

41. Thielicke, W. 2014. The Flapping Flight of Birds - Analysis and Application. .

bioRxiv preprint doi: https://doi.org/10.1101/259778; this version posted February 6, 2018. The copyright holder for this preprint (which was not certified by peer review) is the author/funder, who has granted bioRxiv a license to display the preprint in perpetuity. It is made available under a CC-BY-NC-ND 4.0 International license.

Figure 1, experimental setup: **A)** Diagram of the *in-vitro* system consisting of a supported lipid bilayer (orange), actin-membrane linker protein His10-KCK-FzmABD (HSF, dark grey and red), actin filaments (gray) and muscle myosin II filaments (blue), arrows indicate principle of iSCAT microscopy. **B-C)** Example images of actin filaments (B) and myosin II filaments (C) recorded with a 445 nm laser iSCAT system; scale bar: 2 µm. **D)** Histogram depicting the interferometric contrast distribution along actin filaments (grey, N_{fil}=12, $N_{measure}$=562) and myosin II filaments (blue, N_{fil}=5, $N_{measure}$=96).

Figure 2, dynamics of membrane tethered actin filaments within an actin network: **A)** Example of tracking an single actin filament (red dashed line, l = 0.4 µm) inside an actin network imaged over 120 s (dark blue: 0 s); scale bar: 1 µm. **B)** Corresponding trajectory of the filament in (A) over time, small dots depict the tracked filament, diamonds its center of mass, color indicates time (dark blue: 0 s). **C)** Mean square displacement of the filament's center of mass shown in (B). **D)** Box plot comparing the diffusive behavior (characterized by logarithmic slopes of MSD plots) of short (<1.5 um, N = 25) and long (> 1.5 um, N = 14) actin filaments. **E)** Trajectory of a 4 µm long actin filament confined by the surrounding actin network, small dots depict the tracked filament, diamonds its center of mass, color indicates time (dark blue: 0 s). **F)** Mean square displacement of the filament's center of mass shown in (E), indicating free diffusion at time scales <10 s (logarithmic slope of 1) and confinement at time scales >10 s (logarithmic slope < 1).

Figure 3, myosin II filament dynamics in the acto-myosin network at different ATP concentrations: **A)** Histogram of myosin II filament dwell times to actin at 100 µM ATP (N=6400). **B-D)** Histograms of the myosin II filament velocities (B), run lengths (C) and frequency plot of run length vs dwell time (D) extracted from a subset of the myosin II filament kymographs at 100 µM ATP (N=432). **E)** Histogram of myosin II filament dwell times to actin at 10 µM ATP (N=8000). **F-H)** Histograms of the myosin II filament velocities (F), run lengths (G) and frequency plot of run length vs dwell time (H) extracted from a subset of the myosin II filament kymographs at 10 µM ATP (N=1133). Red lines depict best fits computed with the MEMLET fitting routine: double exponential decay function in (A and E), double Gaussian fit in (B), Gaussian fit in (F) and single exponential decay functions in (C and G). Data displayed in (D and H) was limited to binding times of 10 s to focus on details in this dwell time regime. **I, J)** Schematic depicting two possible modes of myosin filament binding to actin and the corresponding dynamics: (I) one sided binding of myosin II filaments results in short dwell times (τ_1) and high myosin II filament velocities; (J) binding of both sides of the myosin II filament leads to long dwell times (τ_2) and stalled myosin II filaments.

Figure 4, dynamics of contracting acto-myosin networks: **A)** Image sequence depicting the dynamics of a membrane bound acto-myosin network at the contractile state; images were acquired with the 445 nm laser iSCAT setup; experimental conditions: [actin] = 250 nM, [capping protein] = 0.5 nM, [myosin II] = 30 nM, $[ATP]_0$ = 100 µM; scale bar: 5 µm. **B)** Standard deviation (sdv) maps indicating the temporal change in each pixel of the acto-myosin network at different time points representing the remodeling state (60-180 s), short scale clustering (480-600 s) and the contractile state (900-1200 s); scale bar: 5 µm. **C)** Overlay of a snapshot of a contracting acto-myosin network and the vector flow field averaged over 20 s (purple) computed by PIV. **D)** Divergence map computed from (C) indicating regions of contractility (blue regions = negative divergence) co-localizing with acto-myosin clusters. **E)** Overlay of a snapshot of a remodeling acto-myosin network and the vector flow field averaged over 20 s (purple) computed by PIV. **F)** Divergence map computed from (E) showing the absence of contractile regions and sustained network flows. **G)** Histogram of the acto-myosin network flow velocity distribution in the remodeling state (100 µM ATP) and the contractile state (10 µM ATP). Scale bars in C-E: 2 µm.

bioRxiv preprint doi: https://doi.org/10.1101/199778; this version posted February 6, 2018. The copyright holder for this preprint (which was not certified by peer review) is the author/funder, who has granted bioRxiv a license to display the preprint in perpetuity. It is made available under a CC-BY-NC-ND 4.0 International license.

Figure 5, sustained acto-myosin vortices on SLBs: A) Example of an acto-myosin vortex visualized by a minimum projection of a 120 s image sequence (Video 5; scale bar 1 µm. **B)** Corresponding velocity map averaged over 120 s computed with PIV. **C)** Radial profile of the vortex velocity field shown in (G) (black: individual data points, red: averaged data). Experimental conditions in (C-H): [actin] = 300nM, [myosin II] = 80 nM.

Sup Figure 1, detection and identification of actin and myosin II filaments: A) Histogram of myosin II filament length measurements with the 635 nm and 445 nm laser iSCAT set-ups; blue line depicts fit of normal distribution; N = 269. **B)** Single actin filaments landing afresh on the glass slide or moving inside the actin network are visualized by subtracting the median of the image sequence from the raw images; 445 nm laser set-up, scale bar: 1 µm. **C)** Histogram of actin filament contrast measurements with the 445 nm laser iSCAT setup, and fit of the first peak corresponding to the single actin filament signal. **D)** Image sequence of an actin filament landing on top of another imaged with the 445 nm iSCAT setup. **E)** Corresponding measurement of the interferometric contrast of the region depicted by the white box in (D) showing a step-wise increase of the signal corresponding to the actin filament landing on top of another. **F)** Histogram of the actin layer thickness in a typical experiment based on back ground subtracted, local interferometric contrast measurements divided by the average contrast value of an individual actin filament (C) (N=149).

Sup Figure 3, myosin filament dynamics: A) Image sequence showing the run of two myosin II filaments (black) on actin filaments; 635nm laser iSCAT setup, scale bar: 1 µm. **B)** Corresponding kymograph obtained along the red line in (A), black regions correspond to myosin II filaments that are moving along actin filaments; time color bar: 36 s, scale bar: 1 µm. **C)** Rescaled frequency plot of run length vs binding time from (Fig. 3DF) to highlight the short run lengths at 100 µM ATP.

Video 1 Movie showing the increase in interferometric scattering when one actin filament lands on top of another depicted in Sup Fig 2A, B

Video 2 Movie showing the actin filament depicted in Fig 2C

Video 3 Movie showing myosin II filament motion along actin filaments as analyzed in Fig3 and Sup Fig 3

Video 4 Movie showing the transition of the acto-myosin network from a remodeling to a contractile state as analyzed in Fig 4A, B.

Video 5 Movie showing the myosin II filament dynamics forming a vortex analyzed in Fig 4F-H; interferometric scattering signal was inverted and images were converted into 8-bit format for analysis in PIVlab.

Video 6 A second example of vortex formation of myosin II filaments.

Video 7 Movie showing the dynamics of myosin II filaments during transient and partial vortex formation followed by their fusion into a larger, contractile structure.

FIGURE 1

bioRxiv preprint doi: https://doi.org/10.1101/199778; this version posted February 6, 2018. The copyright holder for this preprint (which was not certified by peer review) is the author/funder, who has granted bioRxiv a license to display the preprint in perpetuity. It is made available under a CC-BY-NC-ND 4.0 International license.

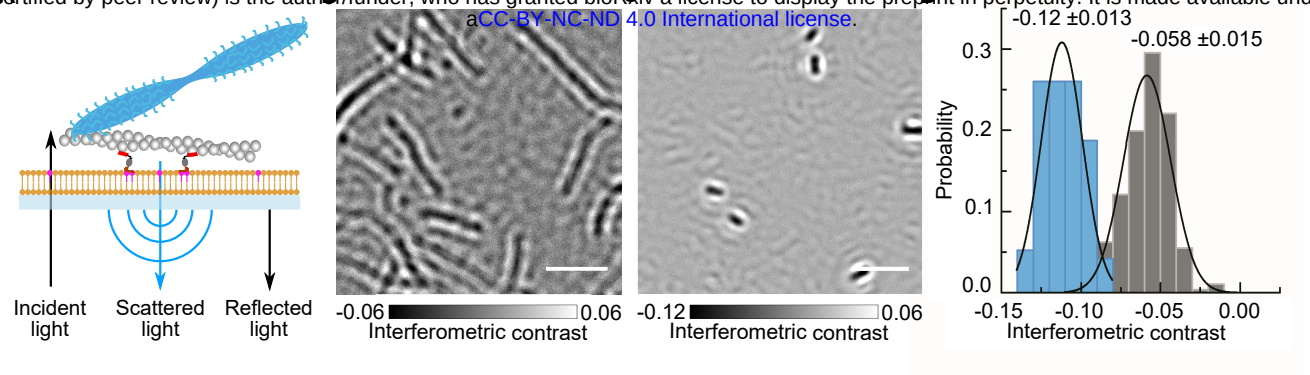

Figure 2

bioRxiv preprint doi: https://doi.org/10.1101/198778; this version posted February 6, 2018. The copyright holder for this preprint (which was not certified by peer review) is the author/funder, who has granted bioRxiv a license to display the preprint in perpetuity. It is made available under a CC-BY-NC-ND 4.0 International license.

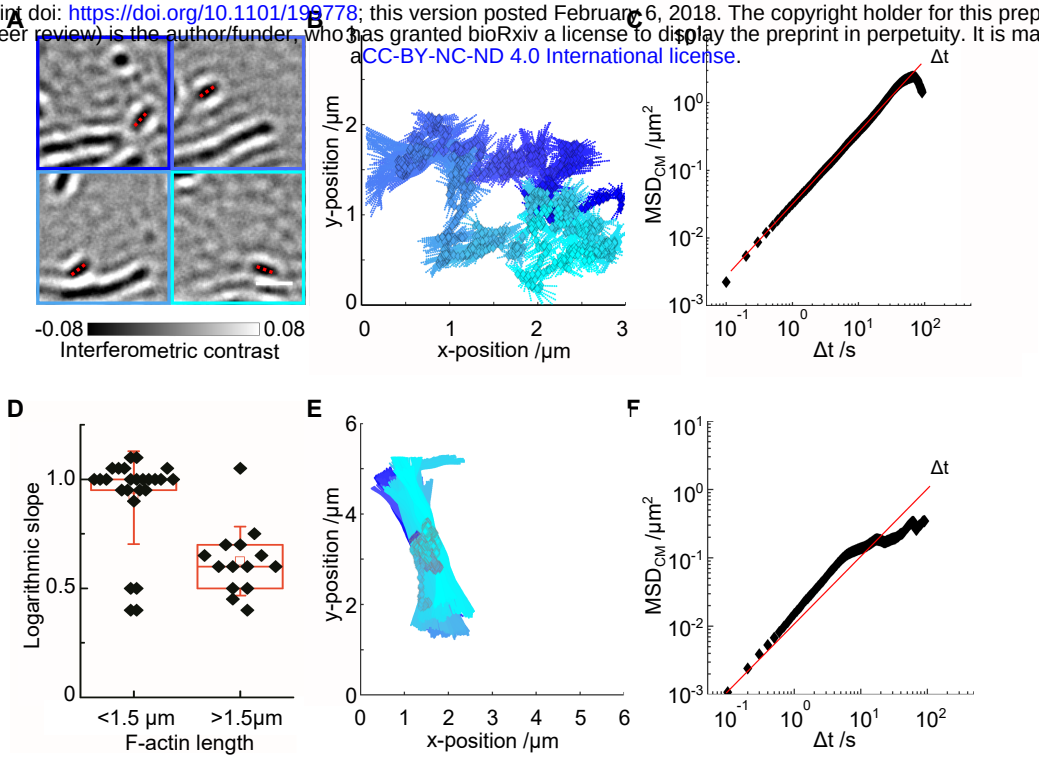

Figure 3

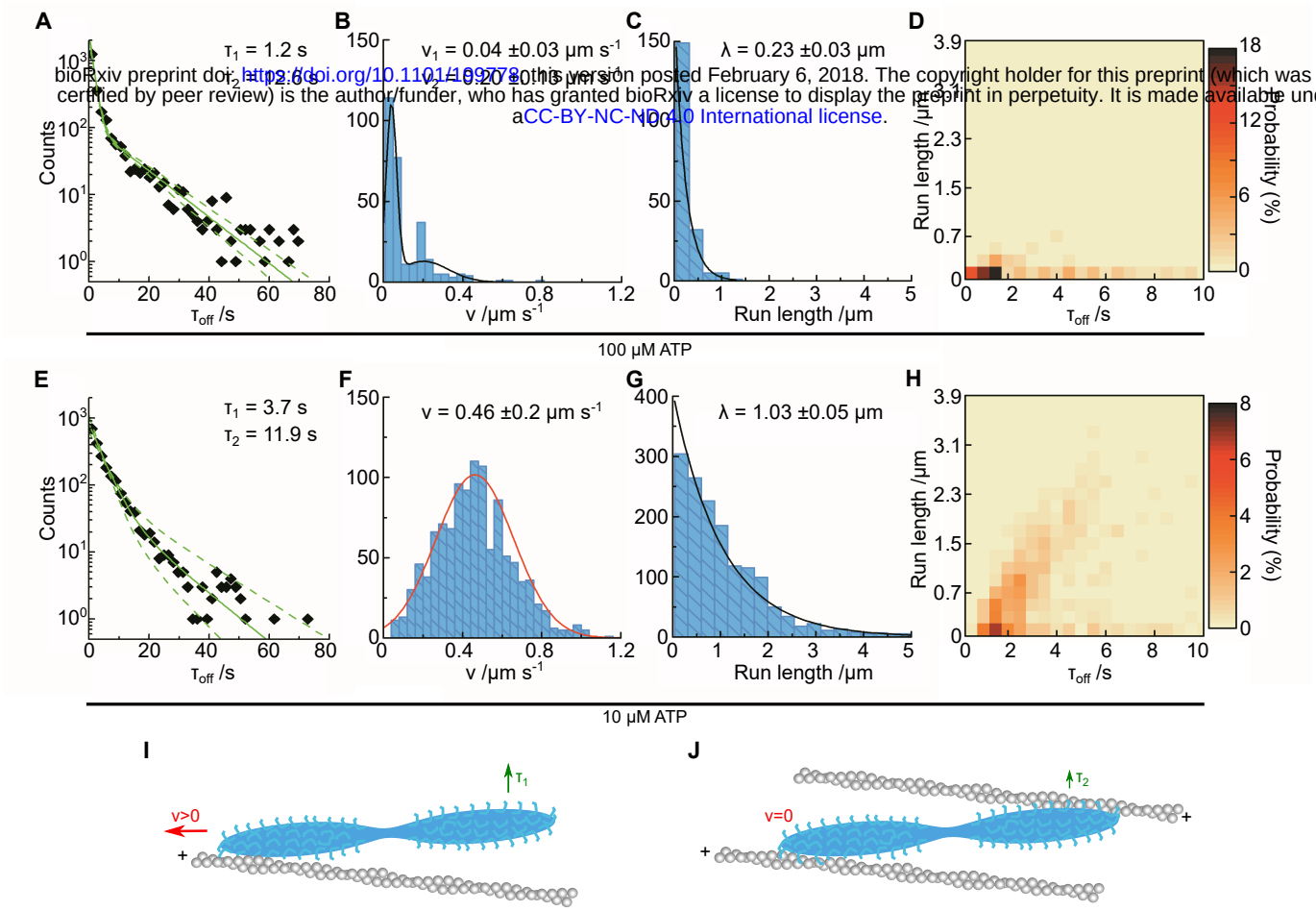

bioRxiv preprint doi: https://doi.org/10.1101/199778 this version posted February 6, 2018. The copyright holder for this preprint (which was not certified by peer review) is the author/funder, who has granted bioRxiv a license to display the preprint in perpetuity. It is made available under aCC-BY-NC-ND 4.0 International license.

Figure 4

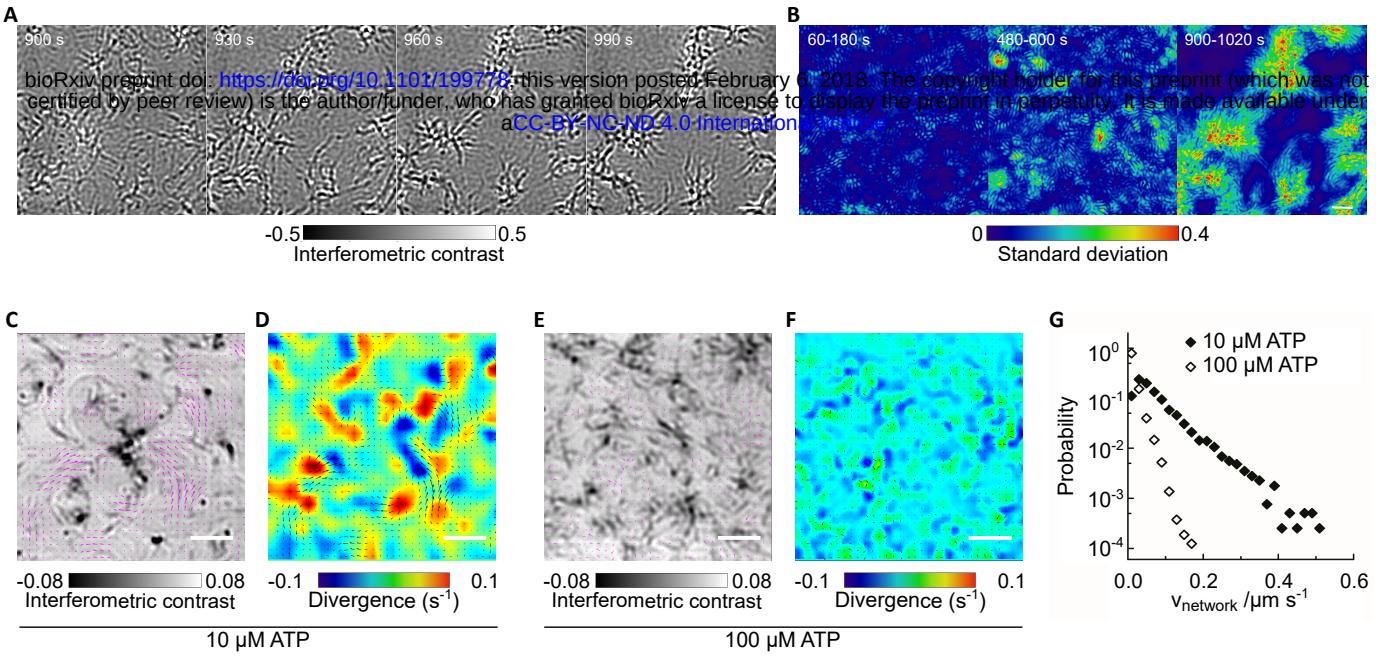

bioRxiv preprint doi: https://doi.org/10.1101/199778; this version posted February 6, 2018. The copyright holder for this preprint (which was not certified by peer review) is the author/funder, who has granted bioRxiv a license to display the preprint in perpetuity. It is made available under aCC-BY-NC-ND 4.0 International license.

Figure 5

bioRxiv preprint doi: https://doi.org/10.1101/199778; this version posted February 6, 2018. The copyright holder for this preprint (which was not certified by peer review) is the author/funder, who has granted bioRxiv a license to display the preprint in perpetuity. It is made available under aCC-BY-NC-ND 4.0 International license.

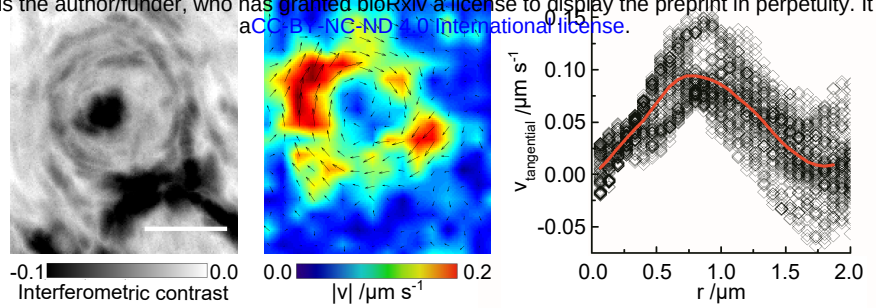

Sup Figure 1

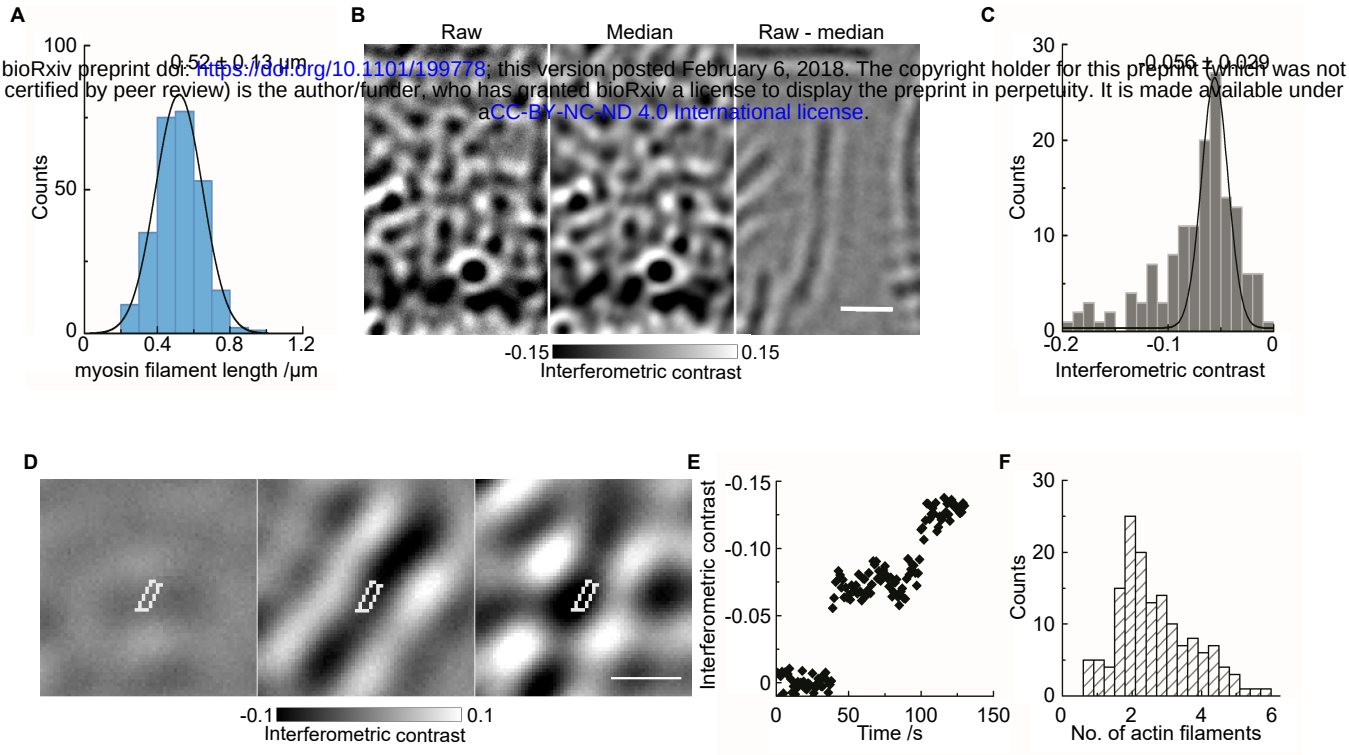

bioRxiv preprint doi: https://doi.org/10.1101/199778; this version posted February 6, 2018. The copyright holder for this preprint (which was not certified by peer review) is the author/funder, who has granted bioRxiv a license to display the preprint in perpetuity. It is made available under aCC-BY-NC-ND 4.0 International license.

Sup Fig 3
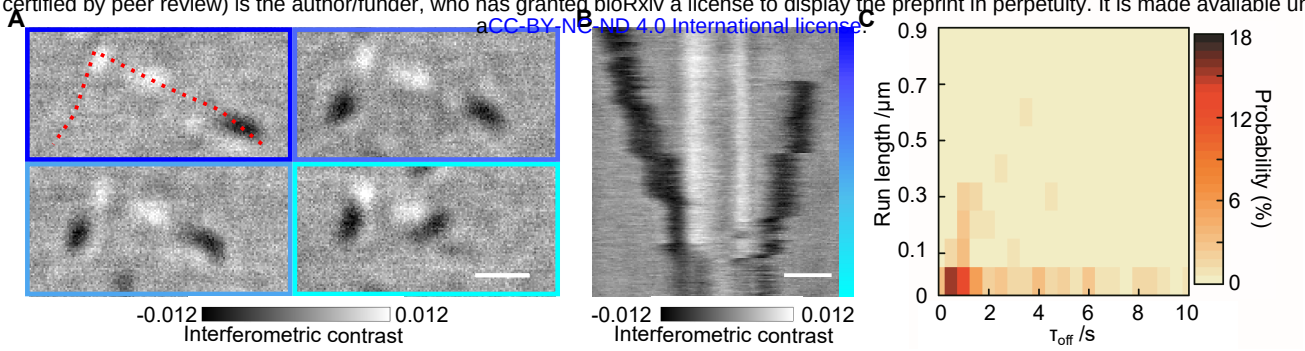
bioRxiv preprint doi: https://doi.org/10.1101/199778; this version posted February 6, 2018. The copyright holder for this preprint (which was not certified by peer review) is the author/funder, who has granted bioRxiv a license to display the preprint in perpetuity. It is made available under aCC-BY-NC-ND 4.0 International license.